ADVANCED MATERIALS TECHNOLOGIES
www.advmattechnol.de

Current Compliance-Driven Morphological Evolution of Conductive Filaments in ECM Cells: Mechanisms, Switching Regimes, and Thermal Effects

*Milan Buttberg, Christina Schindler, Ilia Valov, and Stephan Menzel**

Electrochemical metallization (ECM) cells are a key candidate for emerging applications in neuromorphic computing and in-memory computing, where precise control over switching dynamics is essential. A major challenge in understanding ECM switching behavior lies in accurately modeling conductive filament evolution, particularly side growth. In this study, the first physical continuum model is presented capable of explaining side growth while incorporating all key mechanisms, including redox reactions at interfaces, ion drift, tunnel currents, mechanical stress, active electrode dissolution, Joule heating, and additional tunnel barrier heating. By accounting for these coupled effects together with a moving mesh algorithm for conductive filament growth, the model captures diverse filament morphologies, which play a crucial role in relaxation times of volatile ECM cells and RESET kinetics in non-volatile ECM cells. The results provide important insights into filament formation dynamics, with implications for optimizing ECM-based memory technologies in neuromorphic and in-memory computing.

1. Introduction

Over the last two decades, interest in resistive memory cells has surged, driven by advancements in neural network technology and emerging paradigms such as in-memory computing[1] and neuromorphic computing[2] Electrochemical metallization (ECM) cells - also called conductive bridge random access memory (CBRAM) - are a type of redox-based resistive memory first reported in the late 1990s and early 2000s,[3–5]whereas the electrochemical memory principle was discovered in the mid-1970s.[6,7] ECM cells are particularly attractive due to their volatile and non-volatile switching characteristics—even within the same device—, potential for multi-state behavior, low power consumption, and nanosecond-scale switching speed.[8] They are suitable as both selectors[9] and memory cells in memory applications.[10] The basic structure of an ECM cell, a two-terminal device, comprises three layers: an electrochemically active electrode (AE), typically Ag, Cu, Ni, Te, Co, or Ti,[11–16] and a counter electrode (CE), whose species do not participate in filament formation and are commonly W, Pt, Ti, TiN, or Ru;[11,12,17] and a nanometer-thin switching layer seperating the electrodes.[18,19] This switching layer must be ionically conductive to facilitate the migration of ions from the electrochemically soluble AE material.[20] Various materials have been reported for the switching layer, including metal oxides,[14,21–23] chalcogenides,[12,24–26] 2D materials such as h-BN,[13,27–29] and organic compounds.[30,31]

The resulting ECM cell characteristics—endurance, retention, and variability—depend strongly on the chosen material stack,[8,19] particularly the interplay between the switching layer and the ion-supplying active electrode. An additional important consideration is the trade-off between volatility and LRS: while a stable LRS is typically achieved only at low resistance values, increasing the LRS often leads to volatile behavior.[32–36] The counter electrode also exhibits a catalytic influence on the switching behavior.[11]

Applying a positive voltage at the AE oxidizes AE atoms, partly dissolving the AE and injecting them as ions into the switching layer, where they migrate toward the CE. Once a stable nucleus forms on the CE, the AE^+ ions preferentially reduce onto this initial nucleus, promoting the growth of a conductive path between the AE and CE,[18,37] called conductive filament. Consequently, the ECM cell transitioned to the low resistive state (LRS). In certain cases, multifilamentary switching was also observed.[38] The

M. Buttberg
Institute of Materials in Electrical Engineering and Information Technology II
RWTH Aachen University
Sommerfeldstraße 24, 52074 Aachen, Germany
C. Schindler
Laboratory for Microsystems Technology
University of Applied Sciences
Lothstraße 34, 80335 Munich, Germany
I. Valov, S. Menzel
Forschungszentrum Jülich GmbH
Peter Grünberg Institute (PGI 7) and JARA-FIT
Wilhelm-Johnen-Straße, 52428 Jülich, Germany
E-mail: st.menzel@fz-juelich.de

The ORCID identification number(s) for the author(s) of this article can be found under https://doi.org/10.1002/admt.202500837

DOI: 10.1002/admt.202500837

applied voltage acts as the primary driving force for conductive filament growth. This process continues until the gap between the conductive filament tip and the AE becomes sufficiently narrow, and the conductive filament area expands enough to support a substantial tunneling current. Depending on the current compliance I_{CC} and the material system, conductive filament growth may either stabilize in a tunneling regime or approach a physical contact with the AE, resulting in a wide range of tunable LRS values, also referred to as multilevel switching. The observation of quantized LRS steps below the contact resistance of $R_c = h/2e^2 \approx 12.9\ \mathrm{k\Omega}$ strongly indicates the formation of a quantum point contact between conductive filament and AE.[39–41] Thus, a tunneling regime above a cell resistance of R_c is suggested and a quantum point contact below.[42] Lateral expansion of the conductive filament is reported to be constrained by self-induced mechanical stress.[43–45]

The lifetime of conductive filaments can range from tens of nanoseconds[46,47] to several years.[18] Typically longer lifetimes are associated as non-volatile LRS states and shorter lifetimes as volatile LRS states. For the RESET operation to bring a non-volatile LRS state back to the high resistive state (HRS), a negative voltage is applied to the AE, thus, the redox reactions are reversed and the conductive filament dissolves, either by retracting from the AE in case of a tunneling regime,[48] or by hourglass-shaped constriction and subsequent retraction in case of a galvanic contact.[44] For volatile LRS states, the conductive filament undergoes surface-limited self-dissolution,[49] typically called relaxation.

To prevent thermal breakdown of the cell, external resistors or current limitation techniques are employed to restrict the maximum current, reducing the cell voltage and slowing down further conductive filament growth. Consequently, the conductive filament morphology critically determines the LRS value and, by extension, the conductive filament's lifetime. The LRS is a key performance parameter in resistive switching devices, and its value depends critically on I_{CC}. Variations in I_{CC} significantly impact the final LRS, with higher compliance currents generally resulting in lower LRS states, while lower compliance currents yield higher LRS states. A direct characterization of the morphology is inferred from the conductive filament's radius, assuming a correlation between the lifetime and the radius[49,50] with Herring's scaling law.[46]

Various models have been proposed to elucidate filament growth using distinct methodological frameworks. Kinetic Monte Carlo (KMC) models have demonstrated a wide range of conductive filament morphologies[51,52] and can explain multilevel switching through both the reduction of the gap and the lateral side growth of the conductive filament.[51] However, this comes at the expense of substantial computational effort and results that are numerically challenging to integrate into continuum or compact models. In non-KMC models, the conductive filament morphology is typically predefined as hourglass,[49] cone,[44,50,53,54] or cylinder,[18,55,56] potentially allowing for a variable radius and, consequently, lateral side growth.[43,54] These models demonstrating lateral side growth often lack a comprehensive approach, typically by overlooking redox reactions at the interfaces, assuming constant contact conditions, neglecting tunneling currents between AE and conductive filament, or relying on added driving force to motivate side growth. Moreover, since the electric field in ECM cells is primarily vertical between the two electrodes, a lateral field must be assumed to account for side growth. Yet, no model consistently incorporates all of these effects while providing a comprehensive explanation for side growth. Additionally, the dissolution of the active electrode, leading to the formation of a void-like region, is largely neglected.

In this study, we build upon our previously published model[45] by incorporating AE dissolution, which leads to the formation of a void region in the dissolved domain. This void region inhibits further vertical conductive filament growth due to the absence of electrochemical activity, making lateral conductive filament expansion more favorable, even in the presence of lateral mechanical stress. Additionally, tunnel barrier heating effects, combined with AE dissolution and mechanical stress, are proposed to explain the emergence of diverse conductive filament morphologies observed in experiments, ranging from thin, cone-shaped filaments to wider, bulkier, and cylindrical structures.[23,38,57–63] Since our model can simulate the radius, it offers a novel approach to understanding multilevel switching, as well as variations in RESET and relaxation times.

2. Physical Model

In this study, a previously published 2D axisymmetric continuum model was modified.[45] The model consists of three layers: an electrochemically active top electrode (AE), a solid, purely ion-conducting switching layer, and an inert counter electrode (CE). The fourth layer, used as a linear resistor for current limitation, was modified to also exhibit non-linear behavior to act as ideal current limitation, in experiments often realized as a series transistor. Only the current limitation mode was used during this study. Four distinct growth modes have been reported,[20] characterized by combinations of high and low ion injection rates with high and low ionic conductivity of the switching layer. The model presented in this study can reproduce two of these modes: high and low ion injection rates with high ionic conductivity, leading to conductive filament growth from the CE toward the AE. Both modes result in conductive filament formation at the CE,[64,65] with the critical nucleus at the switching layer/CE interface modeled as a quadrant of a circle with the size of a metal atom. In contrast, for the other two growth modes, the growth direction can be reversed, leading to conductive filament growth from the AE to the CE. It is assumed that forming has already occurred, and all SET and RESET events are subsequent, with each SET starting with a stable nucleus on the CE after full conductive filament dissolution. This assumption is validated by kinetic switching rate experiments, where the slope at low voltages indicates nucleation limitation, contradicting the presence of a remnant conductive filament on the CE.[11] Quantized conduction effects are neglected in the scope of this model.

In the following, the most important equations for conductive filament growth in the presented model will be shown. Further explanations of the equation system and all boundary conditions can be found in Section S1 (Supporting Information). The growth of the conductive filament is described by using Faraday's Law[66]

$$\frac{\partial n}{\partial t} = -\frac{M_{AE}}{z_c e \rho_{AE}} J_{BV} \tag{1}$$

where $\partial n/\partial t$ is the normal conductive filament growth velocity, M_{AE} is the molar mass of the AE material, z_c is the ion charge number, e is the elementary charge, ρ_{AE} is the density of the AE material and J_{BV} is the ionic current density. The ionic current density is described by the Butler-Volmer equation[66,67]

$$J_{BV} = J_0\left(\exp\left(\frac{(1-\alpha)z_c e}{k_B T}\Delta\varphi\right) - \exp\left(-\frac{\alpha z_c e}{k_B T}\Delta\varphi\right)\right) \quad (2)$$

where α is the charge transfer coefficient, T is the local temperature, $\Delta\varphi$ is the overpotential, and J_0 is the exchange current density, defined as

$$J_0 = z_c e c_{ion} k_0 \exp\left(-\frac{\Delta G_A}{k_B T}\right) \quad (3)$$

where c_{ion} is the ion concentration, k_0 is the heterogeneous rate constant, and ΔG_A is the activation energy. The conduction mechanism within the switching layer is assumed to be governed purely by ionic transport, specifically ion hopping stimulated by the applied electric field, as described by the Mott-Gurney law[68,69]

$$\sigma_{ion} = 2 z_c e c_{ion} f_{hop} a_{hop} \exp\left(-\frac{\Delta G_{hop}}{k_B T}\right) \sinh\left(\frac{a_{hop} z_c e \vec{\mathbf{E}}}{2 k_B T}\right)\vec{\mathbf{E}}^{-1} \quad (4)$$

where f_{hop} is the attempt frequency, a_{hop} is the hopping distance, ΔG_{hop} is the hopping energy, and $\vec{\mathbf{E}}$ is the local electric field.

Electronic tunneling currents between the conductive filament and the AE are described using the linearized Simmons tunnel equation. Assuming a trapezoidal barrier, the resulting tunneling current density writes as follows:[70,71]

$$J_{Tu} = \frac{\sqrt{2m^*\Delta W_0}}{2g}\left(\frac{e}{h}\right)^2 \exp\left(-\frac{4\pi g}{h}\sqrt{2m^*\Delta W_0}\right) V_{Tu} \quad (5)$$

where m^* is the effective electron mass, g is the gap distance between conductive filament and AE, ΔW_0 is the tunnel energy barrier, V_{Tu} is the voltage between the filament tip and the AE, and h is the Plank's constant.

The conductive filament is composed of the same material as the AE, though its spatial dimensions are generally reduced to scales below the mean free path of electrons in the AE bulk material. As observed filaments are mostly structurally irregular with defects, scattering effects limit the conductivity. Accordingly, the Fuchs-Sondheimer model is used to modify the specific conductivity of the conductive filament as follows:[72,73]

$$\sigma_{CF} = \sigma_{AE}(T)\,\frac{1+p}{1-p}\,\frac{d}{\lambda_e} \quad (6)$$

where σ_{AE} is the specific conductivity of the AE material, p is a coefficient expressing the magnitude of scattering at the surface of the conductive filament domain, λ_e is the mean free path of electrons in the AE material, and d is the local diameter of the conductive filament.

To avoid thermal breakdown of a device, experiments typically employ a resistor or current compliance to limit the current through the device. In this study, an ideal current source was implemented as an additional layer on top of the cell stack, featuring a voltage-dependent non-linear conductivity to simulate an ideal current source. The non-linear current $I_{R_{NL}}$ through this layer is calculated as follows:[74]

$$I_{R_{NL}} = I_{CC}\left(1 - \exp\left(\frac{V_{R_{NL}}}{V_0}\right)\right) \quad (7)$$

where I_{CC} is the maximum allowed current through the cell, $V_{R_{NL}}$ is the voltage drop across the non-linear resistive layer and V_0 is a fitting factor. To model the thermal properties of the ECM cell, the well-known heat equation is solved across all cell domains, excluding the non-linear resistive layer. All electrical and thermal conductivities are temperature-dependent, governed by first-order and, where applicable, second-order temperature coefficients as described by the equation:

$$\xi(T) = \xi_0 / \left(1 + \alpha\left(T - T_0\right) + \beta\left(T - T_0\right)^2\right) \quad (8)$$

where $\xi(T)$ is the resulting electrical or thermal conductivity, ξ_0 is the electrical or thermal bulk conductivity at reference temperature T_0, α is the first order temperature coefficient and β is the second order temperature coefficient.

2.1. Mechanical Stress Modification

A nanotemplate for preferred conductive filament growth is assumed, potentially caused by electroforming, amorphous thin films, grain boundaries, dislocations, lattice defects, or electrode interfaces. This nanotemplate is implemented by the assumption of lateral mechanical stress during conductive filament formation. The implementation of lateral mechanical stress in the original model[45] was revised from a physical approach to an exponential fitting approach. This modification was undertaken to enhance numerical stability, particularly in conjunction with the moving mesh algorithm. The modified mechanical energy barrier in exponential form is calculated according to

$$\Delta W_{mech} = W_{m,0}\left(\exp\left(\frac{r}{r_{tem,exp}}\right) - 1\right) \quad (9)$$

where r is the radial coordinate and $r_{tem,\,exp}$ is a fitting constant. This form fulfills the requirements of $\Delta W_{mech} = 0$ for $r = 0$. The similarity between the two approaches in the vicinity of the conductive filament indicate that the exponential approach can be used without compromising the accuracy of the model. Further details can be found in Section S2 (Supporting Information).

2.2. Thermal Modeling

Due to the significantly higher magnitude of the tunneling current compared to ionic currents, Joule heating is considered in all metallic domains but is neglected within the switching layer. Nevertheless, the heat equation is solved across all domains. Additionally, energy relaxation of tunneling electrons is accounted

for, resulting in additional heat dissipation at the conductive filament/switching layer and switching layer/AE interfaces. The resulting power density q_{Tu} at the respective electrodes is calculated as:[75]

$$q_{Tu} = \gamma(V) V_{Tu} J_{Tu} \tag{10}$$

where $\gamma(V)$ is a dimensionless coefficient <1 that describes the distribution of power density between the electron-receiving and electron-emitting electrodes. Typically, more energy is dissipated at the electron-receiving electrode. Further details can be found in Section S3 (Supporting Information).

2.3. Dissolution of the Actice Electrode

The application of Equation (1) and a moving mesh to the switching layer-AE interface results in a homogeneous dissolution of the AE at the same rate as the tip of the conductive filament. Consequently, the gap between the AE and conductive filament would remain constant. However, experimental TEM images indicate clear localized dissolution of the AE above the conductive filament.[61] This strong localization can be attributed to ions taking the shortest path from AE to the reduction site, and to charge accumulation within the switching layer, far from the reduction site, which inhibits further dissolution and ion injection. Since our model lacks charge accumulation, we compensate by mirroring conductive filament growth to the switching layer/AE interface. This results in the conductive filament being depicted as a negative in the AE, maintaining a constant gap between conductive filament and AE. To achieve a closing gap, a linear constant $\nu^* < 1$ is introduced to reduce the dissolution speed of the AE. This adjustment is necessary due to the surface asymmetry between the conductive filament and the AE, as well as the axial symmetry of the system. Additionally, since the model does not explicitly simulate ion movement, this parameter acts as a compensation factor. When the AE dissolves, resulting into a void region, no more electrochemistry is locally possible due to a missing AE/switching layer interface. It is further assumed that only two atomic layers can dissolve into the switching layer, thus leaving a possible minimum void-gap of 0.07–0.4 nm. For the simulated Cu/10 nm-SiO_2/Pt cell from Schindler,[17] a value of $\nu^* = 0.05$ was found.

2.4. Impact of Void Formation in Dissolved Active Electrode Domain

The formation of a void in the AE domain eliminates the switching layer/AE interface, making the application of electrochemical principles invalid and necessitating the suppression of conductive filament growth in this region. A numerically stable implementation, akin to the approach used for mechanical stress, was achieved by modifying the local activation energy in the Butler-Volmer Equation (Equation (2)) with an additional height-dependent energy term. The added energy barrier was calibrated to allow conductive filament growth up to a diameter of one metal atom (≈ 0.2 nm) within the void region. This energy was determined to be $\Delta W_{void} = 0.01$ eV at the original switching layer/AE interface, resulting in the following exponential expression:

$$\Delta W_{void} = W_{v,0} \exp\left(\frac{z}{z_0}\right) \tag{11}$$

where z is the vertical coordinate relative to the original switching layer/AE interface and z_0 is a fitting parameter. Incorporating this vertical energy barrier into Equation (3) yields an effective spatial activation energy:

$$\Delta W_{A,eff}(r,z) = \Delta W_A + \Delta W_{mech}(r) + \Delta W_{void}(z) \tag{12}$$

This expression represents the modified activation energy profile, incorporating both the vertical energy barrier within the void region and the lateral energy barrier induced by mechanical stress.

3. Results

The proposed model is validated and discussed using data from literature, specifically Cu/10 nm-SiO_2/Pt cells.[17] The material system was chosen for modeling, as especially SiO_2 is a well-known material in the semiconductor industry, offering excellent compatibility with existing fabrication processes and well-characterized, albeit moderate, ionic, and electrical properties compared to other possible switching layer materials like e.g., chalcogenides. The simulation parameters used in this study are listed in Section S4, Table S1 (Supporting Information). In addition to validating the model, we compare key aspects of conductive filament growth with and without AE dissolution, as well as the impact of tunnel barrier heating by analyzing cases with and without its inclusion. The following sections present the results and discuss critical switching behaviors, with a particular focus on abrupt and gradual switching mechanisms.

3.1. Multilevel Switching Due to Vertical and Lateral Growth

Figure 1a presents experimental data alongside simulation results depicting the resulting LRS as a function of I_{CC} for an Cu/10 nm-SiO_2/Pt cell. The simulations were conducted using a bias sweep rate of 1 Vs^{-1} with a maximum voltage of V_{max} = 2 V to replicate the experimental conditions accurately. When the conductive filament morphology remains nearly constant and the LRS value changes primarily due to gap reduction, we define this as gap-LRS. Conversely, when side growth results in a wider and bulkier conductive filament – different for each LRS state –, we define it as side-growth-LRS. Figure 1b illustrates the gap evolution over time for both gap-LRS and side-growh-LRS. The inset zoom clearly reveals a slowdown in gap closure during side growth. Figure 1c shows constant conductive filament morphology for low values of $I_{CC} \leq 100$ nA. This value depends on the minimum allowed gap defined by ν^*. It was shown that the simulated morphologies obtained from this type of continuum simulation represent only the filament envelope and lack information about the internal atomic structure. For this type of simulation results, distinct possible atomic configurations have been reported for different switching regimes.[45] In this regime, the conductive filament tip is sufficiently wide to reach I_{CC} solely through

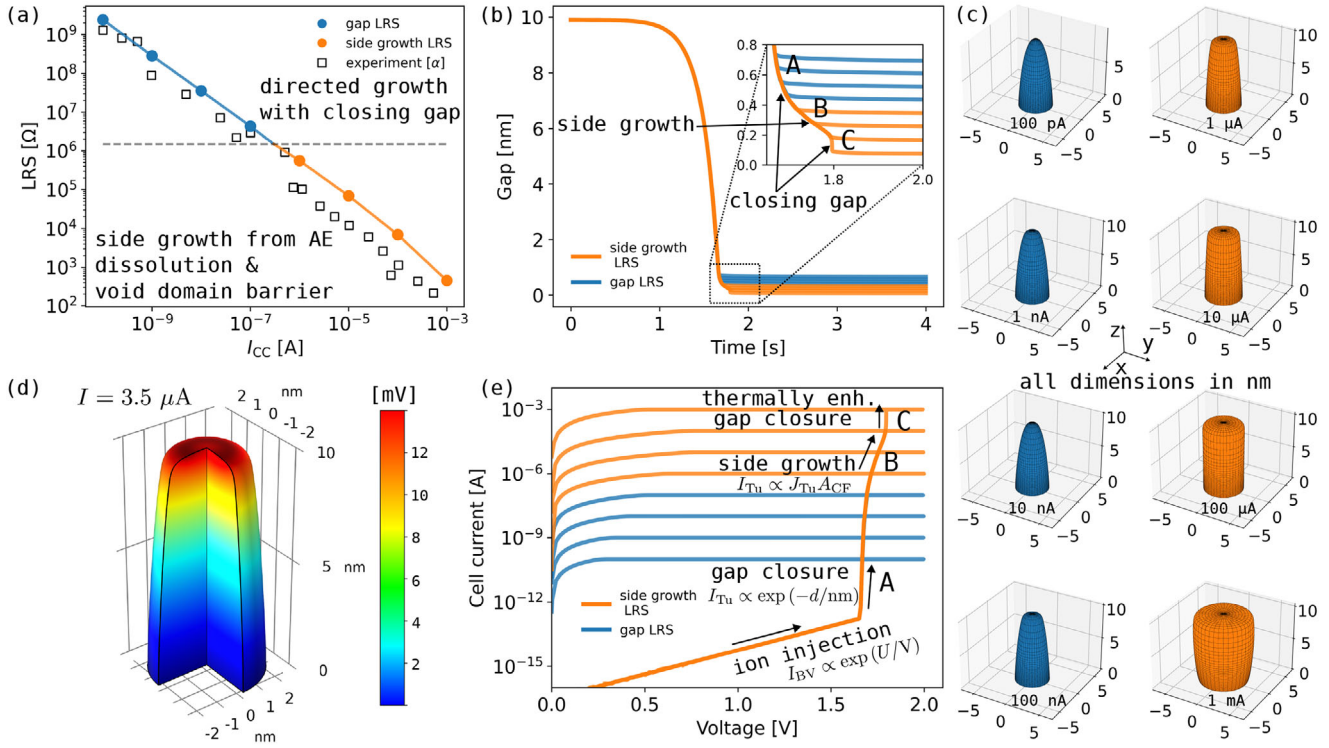

Figure 1. Simulation results for an Cu/10 nm-SiO_2/Pt ECM cell under a triangular voltage sweep (1 Vs^{-1}, max. 2 V): a) LRS as a function of I_{CC}, with distinct states for gap-defined and side-growth-defined LRS. Experimental data [α] from[17] are included for comparison. b) Temporal evolution of the gap, with the inset detailing the final gap states for different I_{CC} values, highlighting the transition from gap closure to side growth and back to gap closure. c) Corresponding conductive filament morphologies for various I_{CC}, illustrating almost constant conductive filament morphologies for I_{CC} < 100 nA and strong side growth above. All dimensions are in nm. d) Snapshot of the voltage drop (in mV) across a conductive filament during the SET process at a momentary current of 3.5 μA, indicating a resistance in the kΩ range. e) *I-V* characteristics for different I_{CC}, showing distinct switching behaviors: abrupt (gap closure), gradual (side growth), and abrupt (gap closure).

gap closure and a voltage drop from the current limitation slows down further conductive filament growth.

However, when I_{CC} increases, the tip area of the conductive filament becomes insufficient to support I_{CC}. If I_{CC} cannot be reached through gap closure alone, the driving force persists within the device, promoting lateral conductive filament growth. Consequently, the tip area expands laterally u ntil the imposed I_{CC} is achieved, while also closing the gap, but at a reduced growth speed. The reduced vertical growth speed is a result of the energetical barrier from the AE dissolution and void formation, but can partly also be attributed to a voltage drop across the conductive filament, thus reducing the overpotential driving the electrochemical reactions.

Assuming an initial monoatomic chain conductive filament with a resistance of $h/2e^2 \approx 12.9\,\mathrm{k\Omega}$, a critical voltage drop on the order of tens of millivolts is already achieved at the microampere range (Figure 1d). Thus, the growth speed of the tip is reduced and conductive filament widening occurs. With the additional energy barrier in the dissolved region, this effect is strongly enhanced.

Both conductive filament growth mechanisms, namely vertical growth and lateral side growth, can be discerned from *I–V* curves (Figure 1e) by analyzing the slope of the current rise. An exponential increase in the cell current reflects a decreasing gap, attributed to the change of the tunneling current $\partial I_{Tu}/\partial g \propto -\exp(-g/\mathrm{nm})$. In contrast, a non-exponential or linear current increase suggests side growth, characterized by $\partial I_{Tu}/\partial r \propto J_{Tu} r$, with r representing the effective filament radius. Regime A exhibits exponential current rise due to a closing gap; Regime B exhibits gradual current increase due to lateral side growth and Regime C exhibits exponential current rise again. While the mechanisms in Regime A and B are straightforward, the behavior observed in Regime C is governed by an electro-thermal coupling effect. At this stage, the conductive filament has grown significantly and already conducts > 100 μA. The tunnel heating effect causes a temperature increase of $\Delta T > 100\,\mathrm{K}$, which accelerates electrochemical reactions at the conductive filament tip. Consequently, the vertical energy barrier – which at this point is lower than the radius-scaling lateral mechanical stress barrier – is reduced sufficiently to be overcome. This leads to renewed conductive filament growth in the vertical direction, now occurring at an accelerated exponential rate due to thermal effects. As a result, a "jump"-like behavior is observed in the gap evolution (Figure 1b) and thus in the depending tunneling current response.

The directed growth of the conductive filament is shown in **Figure 2** in two spatial and one temporal dimension, called "elephant plot" due its characteristic appearance. The growth starts around $\log_{10}(t/s) = 0.05$. Up to this point, isotropic growth occurs within the nanotemplate, after which lateral mechanical constriction induces anisotropic, directed growth, followed by vertical

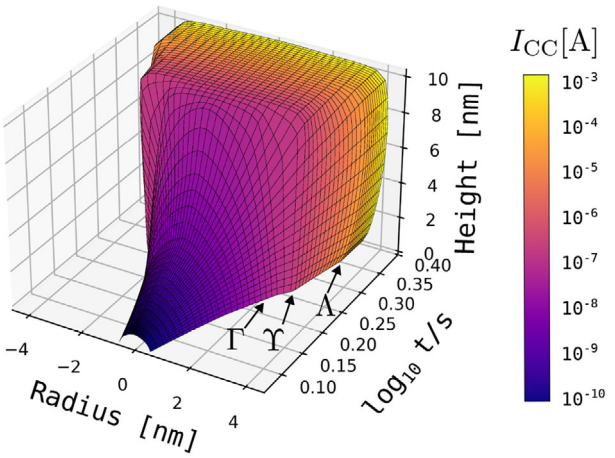

Figure 2. "Elephant plot" illustrating conductive filament growth in space and time for a maximum compliance current of $I_{CC} = 1$ mA. During growth, the filament morphology progresses through all intermediate states corresponding to lower I_{CC}. At point $\Gamma \approx \log_{10}(t/s) = 0.225$, vertical gap closure is inhibited by AE dissolution and resulting void domain, causing lateral expansion to dominate. At point $\Upsilon \approx \log_{10}(t/s) = 0.25$, the maximum current $I_{CC} = 1$ mA is reached, and further growth slows down due to the current compliance limiting the voltage. As a result, lateral expansion decelerates. Minimal thermally activated vertical filament growth continues, leading to further resistance reduction and thus an even stronger voltage limitation. Filament growth becomes unrecognizable at point $\Lambda \approx \log_{10}(t/s) = 0.35$.

constriction due to AE dissolution and void formation at around point Γ. The simulation was conducted for an $I_{CC} = 1$ mA, thus the conductive filament progresses through all intermediate morphologies that depend on I_{CC}. At point Υ the maximum current was reached. Consequently, the current compliance limits the voltage, reducing the growth speed, as evidenced by the slowdown in lateral expansion between points Υ and Λ. Beyond point Λ the voltage is so strongly limited that no further growth is recognizable on this time scale. The region between points Λ and Υ thereby correspond to Regime B from Figure 1b,e. During this time, the conductive filament tip heats up due to Joule heating and tunnel barrier heating. Ultimately, thermally enhanced slight vertical growth occurs. This, in turn, provokes an abrupt current response by decreasing the gap and thus increasing the tunneling current marking the onset of Regime C. Regime C takes place on a very short timescale before point Λ.

Figure 3a–d demonstrates the morphological and temperature evolution of a conductive filament, also with $I_{CC} = 1$ mA, which leads to side growth. The final minimal gap, positioned off-center from the symmetric axis (inset zoom Figure 3d), represents a preliminary stage toward the formation of a quantum point contact, delineating the transition from tunneling to contact. The previously described effect of overcoming the vertical energy barrier via increased conductive filament temperature is clearly illustrated in Figure 3b and 3c.

In the scope of this explanation the atomic switch can be understood as a quantised switching mode, where an atomic contact is made in the void region of the dissolved AE domain. For certain material systems, conductive filaments should grow into the AE by repeatedly forming and rupturing quantum point contacts.

Figure 4a–e, reprinted from Ref. [17], presents such conductive filament growth into the AE for lateral Ag/GeSe samples. A W tip was positioned on the GeSe region, and positive bias was applied to the Ag electrode. Following switching, the image was acquired using SEM. In the magnified progression from (a) to (e), conductive filament growth into the AE is clearly observed, accompanied by significant AE dissolution in the respective region. It should be noted that the conductive filament may have preferentially grown along the sample surface, which could be energetically favored compared to bulk growth. As a result, AE dissolution and conductive filament growth into the AE may appear stronger than in typical, vertical ECM cell stacks with buried conductive filaments. Furthermore, multi-conductive filament growth is clearly visible. The sample dimensions, particularly the isolating material thickness, are orders of magnitude larger than in conventional devices, where thickness typically measures only tens of nanometers. Nevertheless, Figure 4f displays a toggling current response under constant bias with abrupt and gradual change rates, which may suggest the repeated formation and rupture of quantum point contacts during growth into the AE, but also side growth and widening effects (Figure 4a–e). This observation supports our assumption of a preliminary stage of quantum point contact formation and side growth in ECM cells.

Our assumption of side growth is further reinforced by carefully selected experimental *I–V* switching data subsets from the literature.[76–81] These data, plotted in normalized form in Figure 4g, closely align with our simulated switching behavior: an initial exponential current rise due to gap closure, followed by a transition into a gradual increase attributed to side growth, and ultimately a steeper exponential rise driven by thermally activated gap closure and quantum point/ohmic contact formation. A more detailed analysis of these findings is provided in the Discussion section

3.2. Impact of Model Extensions

It was demonstrated that accurate thermal modeling is essential for understanding the switching dynamics in ECM cells, particularly through the implementation of an additional heat source–tunnel barrier heating. **Figure 5**a depicts the maximum temperature reached in the conductive filament during the SET process depending on the maximum current I_{CC}, comparing scenarios with Joule heating alone and with the inclusion of tunnel barrier heating. Without tunnel barrier heating, the temperature increase is negligible, whereas with tunnel barrier heating, an exponential temperature rise with increasing I_{CC} is observed, reaching a maximum conductive filament tip temperature of 850 K for $I_{CC} = 1$ mA. The resulting switching dynamics are compared in Figure 5b. With Joule heating alone, the *I–V* characteristic exhibits an exponential current rise, followed by a transition to linear current rise due to side growth.

However, this growth is too slow to reach I_{CC} under the applied triangular bias signal with a sweep rate of $1\,Vs^{-1}$. In contrast, when tunnel barrier heating is included, I_{CC} is reached, and an abrupt increase in current is observed at approximately 100 µA, consistent with well-known general experimental *I–V* characteristics.

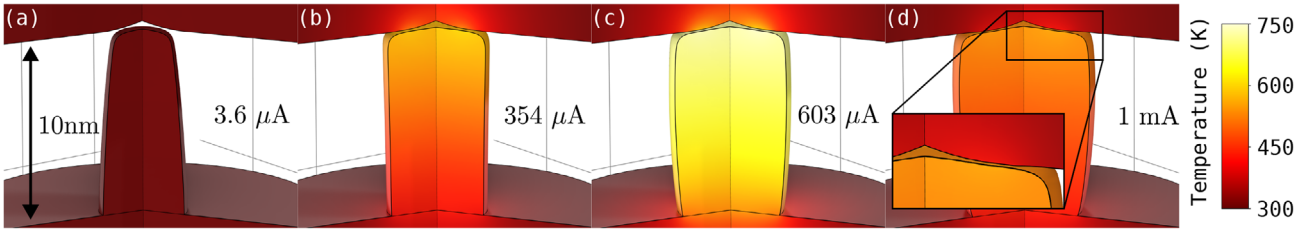

Figure 3. Spatial and thermal evolution of the conductive filament during the SET process at different momentary currents, showing temperature rise from (a) to (c) with a peak temperature of 750 K at (c) for 603 µA. Shortly after reaching I_{CC} = 1 mA in (d), the temperature decreases due to the voltage drop caused by the current compliance. Minimum gap off-centered from symmetric axis in inset zoom in (d).

Figure 5c presents the simulated *I*–*V* characteristics with and without AE dissolution. In the absence of AE dissolution, the cell current exhibits an exponential rise as the gap decreases to infinitesimal, nonphysical values, which occurs when contact formation is not permitted in the model. Consequently, for our set of parameters, I_{CC} = 1 mA leads to infinitesimal gap and a numerical unstable solution, which is why results for I_{CC} = 0.1 mA is shown for gap closure only. When AE dissolution is incorporated, the initial exponential current rise A transitions into a linear increase B, followed by a sharper exponential current rise C enabled by accurate temperature modeling, which includes tunnel barrier heating. Consequently, a physically meaningful gap is maintained throughout the process (Figure 5d).

3.3. Discussion

Our suggestion of side growth is corroborated by reported experimental results, which display an initial exponential current response transitioning into a gradual linear regime, followed by a sharp rise (Figure 4g). Out of the reported experimental data,[76–81] only specific curves were extracted and presented, where side growth is assumed. For instance, in several datasets containing multiple measurements, a small subset of curves supports our findings on conductive filament growth mechanisms for multilevel switching. These mechanisms are characterized during SET by a transition from an exponential current response due to gap closure to a gradual linear current response attributed to side growth, followed by a return to an even faster exponential current response driven by thermally enhanced gap closure. For better recognition, the side growth regime has been highlighted. The selection of specific experimental data not only validates our simulation results, but also highlights the variability in conductive filament tip/AE interaction mechanisms observed in ECM cells, namely vertical conductive filament growth towards the AE with AE dissolution, void formation, gap closure, side growth with and without (this study) abrupt quantum point/ohmic contact formation, all combined with multifilamentary conducting filament growth. These mechanisms are only valid for the aforementioned conductive filament growth modes of high ion mobility and high or low ion injection rates.

Furthermore, the presented results elucidate the distinct mechanisms governing conductive filament growth in ECM cells, specifically the interplay between vertical and lateral growth under varying current compliance I_{CC} and with concurrent dissolution of the AE. Notably, the identification of gap-LRS regimes and side-growth-LRS regimes, as well as the critical role of

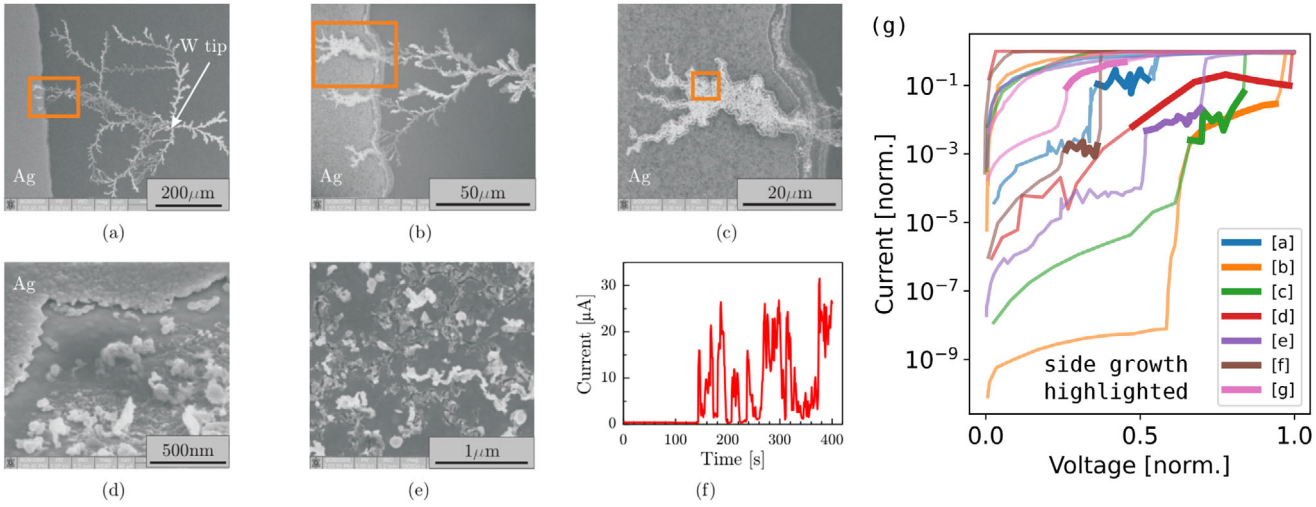

Figure 4. SEM images of conductive filament growth in a planar Ag/AgGeS sample using a W needle as the CE. a–c) Continuously zoomed-in images of conductive filament and the conductive filament/AE interface. d–e) High-magnification views of the dissolved Ag electrode. f) Current response after applying 4 V to the Ag electrode, where current jumps suggest the formation and rupture of quantum point contacts. g) SET pulse data (a, b, e–g) extracted from Refs. [76–80], respectively, and forming pulse data (c and d) extracted from Ref. [81]. a–f) reprinted with permission from Ref. [17].

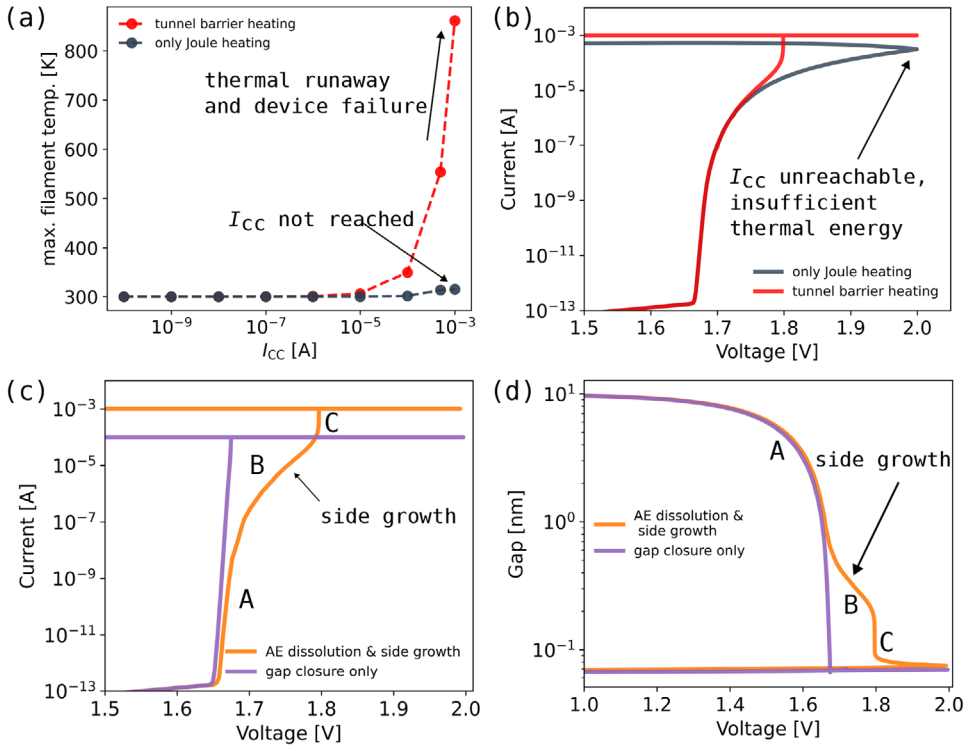

Figure 5. Impact of tunnel barrier heating on device temperature and switching behaviour and impact of AE dissolution on switching behavior and gap evolution. a,b) Impact of tunnel barrier heating: (a) Maximum conductive filament temperature for different I_{CC} values. Without tunnel barrier heating, I_{CC} = 1 mA cannot be reached due to insufficient thermal energy to overcome the void barrier of the dissolved AE. With tunnel barrier heating, higher I_{CC} values lead to thermal runaway and potential device failure. (b) Corresponding *I–V* characteristics for I_{CC} = 1 mA, showing that without tunnel barrier heating, I_{CC} remains unreachable due to inadequate thermal energy. c,d) Impact of AE dissolution: (c) *I–V* characteristics and (d) gap evolution over time, illustrating the effect of AE dissolution. Without AE dissolution, a numerically stable solution for I_{CC} = 1 mA cannot be reached due to the infinitesimal gap; thus, results for I_{CC} = 0.1 mA are shown. Exponential current increase and gap closure A transition to gradual behaviour B, followed by electrothermal activated exponential gap closure and current response C.

thermal effects in driving renewed conductive filament growth at high currents, provides significant insights into the dynamic evolution of conductive filament morphology.

A key observation is the dependence of conductive filament morphology on I_{CC}, which governs the transition between the gap-LRS regimes and side-growth-LRS regimes. At low I_{CC}, the filament reaches the required current through gap closure alone, resulting in minimal lateral growth. However, for higher I_{CC} and the progressing dissolution of the AE–resulting in the formation of a void domain that blocks further vertical growth and gap closure–the conductive filament begins to expand laterally, thereby increasing the effective area for electron tunneling. This lateral side growth manifests as a gradual linear increase in cell current. Subsequently, Joule heating, and in particular tunnel barrier heating, drives further conductive filament growth into the void domain, promoting thermally accelerated gap closure and leading to a faster exponential, jump-like increase in current. At this stage, it is highly likely that a quantum point contact forms, marking a preliminary or transitional phase toward full quantum point contact and eventual ohmic contact formation–a process that our current model is not yet capable of fully capturing.

Nevertheless, a more comprehensive understanding of these mechanisms can be derived from the schematic representation in **Figure 6**, which illustrates *I–V* curves under exponentially increasing I_{CC} and the corresponding conductive filament morphologies at key switching points. This schematic captures the progression from gap-LRS (A)-(F) to side-growth-LRS (G), ultimately leading to thermally activated quantum point contact and/or ohmic contact formation (H). It provides a consolidated overview of the distinct growth regimes and the critical transitions observed in ECM cells.

In particular, the schematic serves as an updated model, highlighting the interplay between vertical and lateral conductive filament growth, void domain formation due to AE dissolution, and the impact of electro-thermal effects on conductive filament dynamics. By visualizing these key processes, the schematic not only reinforces the findings presented but also offers a refined framework for interpreting switching phenomena, including the preliminary stages of quantum point contact formation. Furthermore, the transition to ohmic contact, depicted in the final phase (H), represents an important step toward understanding multilevel switching behavior in ECM devices.

The observed variations in conductive filament growth behavior and the transitions between different LRS regimes are inherently influenced by multiple material and structural factors. These variational factors depend on the thermal, mechanical and ion-conducting properties of the materials involved, particularly

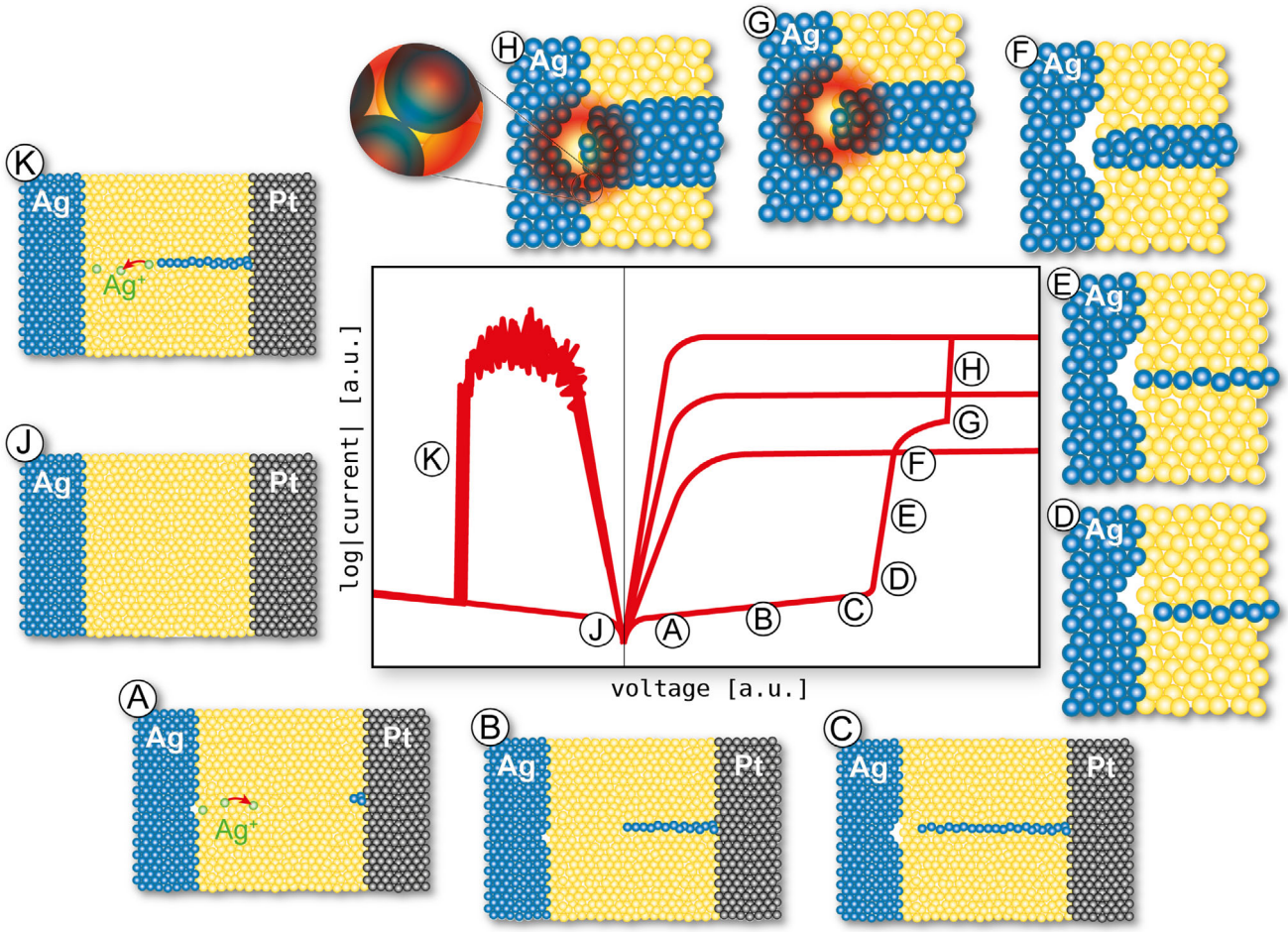

Figure 6. Atomic-scale schematic of conductive filament formation and dissolution in an Ag/SiO_2/Pt ECM cell correlated with sketched *I–V* characteristics for different I_{CC} values. A–C) Initial oxidation and migration of Ag^+ ions toward the Pt electrode with initial nucleus, dissolution of the AE and directed conductive filament growth toward the AE. D–F) Further conductive filament growth blocked by dissolved AE void-like region, resulting in side growth, thus strengthening the conductive filament. G–H) Increasing temperature with increasing I_{CC} due to tunnel barrier heating and thus overcoming the void domain barrier of the dissolved AE region. K–J) Dissolution and retraction of the conductive filament during the RESET process, exhibiting typical variability at the maximum RESET current.

those of the switching layer, as well as the doping concentration, defect density (including lattice defects), and the distribution of grain boundaries within the switching layer, which collectively define the nanotemplate guiding conductive filament growth.

For our studies, we applied the bulk values for thermal conductivity; however, it may be more realistic to consider reduced thermal conductivity due to nanoscale scattering effects. Such a reduction leads to earlier onset of conductive filament heating, thereby shifting the onset of gradual switching to even lower current levels. Moreover, higher maximum temperatures result in increased ionic injection rates, accelerating the switching process. See Section S5 (Supporting Information) for more detailed information and results.

As noted before, the presented continuum model captures only the envelope of the conductive filament and does not resolve its internal atomic structure. As such, complex morphological features frequently observed in high-resolution TEM[23,38,58–61] —such as thin dendritic filaments, or irregular, defect-rich bulky filaments – cannot be directly reproduced. This limitation arises from the mesoscopic nature of the model, which averages over atomic-scale disorder and stochastic effects. Nonetheless, the simulated filament radii and morphology transitions remain physically meaningful for analyzing switching regimes, electrothermal effects, and device-level behavior. This is because, in practice, one filament dominates, and the model captures the growth dynamics of this prevailing conduction path.

Furthermore, different conductive filament morphologies may provide an explanation for the varying RESET kinetics observed in ECM cells, where experimental results have shown discrepancies. In one case, no correlation between LRS and RESET time was reported,[82] while another study observed an exponential dependency, with lower LRS corresponding to higher RESET times.[83] We hypothesize that in the scenario where no correlation between LRS and RESET time was found, multifilamentary conductive filament growth likely occurred, resulting in nearly identical conductive filament morphologies across different LRS states. Conversely, in the case of exponential dependency, distinct conductive filament morphologies were likely present, leading to

varying RESET dynamics depending on the specific conductive filament structure.

Our findings could also be applied to explain the orders of magnitude variations in relaxation times observed in volatile ECM cells.[12,47,84–89] These variations are typically explained using Herring's scaling law, which establishes a relationship between the conductive filament radius r_0 and the relaxation time t_r as $t_r \propto r_0^4$. If applied to our simulation results with an increased average filament radius by approximately a factor of 2, relaxation time variations exceeding an order of magnitude can be explained, depending on the compliance current I_{CC}.

4. Conclusion

This study advances the understanding of conductive filament growth mechanisms in ECM cells by identifying distinct switching regimes and clarifying the role of material properties and electro-thermal effects in conductive filament evolution. The transition from gap-LRS to side-growth-LRS, driven by varying current compliance and AE dissolution, provides a nuanced framework for interpreting switching behavior. A key finding is that side growth at higher current compliance results in varying conductive filament morphologies, with high current compliance leading to wider, bulkier, and cylindrical conductive filaments, while low current compliance produces thinner and/or cone-shaped conductive filaments. Vertical and side growth can be distinguished by their respective *I–V* characteristics: vertical growth, which corresponds to gap closure, exhibits an abrupt, exponential current rise, whereas side growth manifests as a gradual, linear increase in current.

The incorporation of tunnel barrier heating leads to elevated conductive filament temperatures even at low currents, which accelerates further vertical growth once side growth has increased the current to a critical heating level. These morphological differences could help explain discrepancies in RESET kinetics reported in the literature, where both exponential dependencies and the absence of correlation between LRS and RESET time have been observed. Additionally, the insights gained on conductive filament morphology and thermal effects could help explain the orders of magnitude variations in relaxation times observed in volatile ECM cells. Understanding these mechanisms provides a foundation for designing ECM devices with improved relaxation time control. Nevertheless, further experimental validation and refinement of models - especially the formation of a contact between conductive filament and AE - are required to fully capture the complex interplay of thermal, mechanical, and electrochemical factors in ECM cells.

Supporting Information

Supporting Information is available from the Wiley Online Library or from the author.

Acknowledgements

This work was supported by the Federal Ministry of Education and Research (BMBF, Germany) in the project NEUROTEC (Project Nos. 16ME0398K and 16ME0399). It was based on the Jülich Aachen Research Alliance (JARA-FIT).

Open access funding enabled and organized by Projekt DEAL.

Conflict of Interest

The authors declare no conflicts of interest.

Data Availability Statement

The data that support the findings of this study are available from the corresponding author upon reasonable request.

Conflict of Interest

The authors declare no conflict of interest.

Keywords

CBRAM (Conductive Bridge Random Access Memory), conductive filament growth, ECM (Electrochemical Metallization), joule heating, neuromorphic computing, side growth, simulations

Received: April 17, 2025
Revised: August 13, 2025
Published online: September 15, 2025

[1] G. Zhou, Z. Wang, B. Sun, F. Zhou, L. Sun, H. Zhao, X. Hu, X. Peng, J. Yan, H. Wang, W. Wang, J. Li, B. Yan, D. Kuang, Y. Wang, L. Wang, S. Duan, *Adv. Electron. Mater.* **2022**, *8*, 2101127.
[2] J. H. Cha, S. Y. Yang, J. Oh, S. Choi, S. Park, B. C. Jang, W. Ahn, S. Y. Choi, *Nanoscale* **2020**, *12*, 14339.
[3] W. C. West, K. Sieradzki, B. Kardynal, M. N. Kozicki, *J. Electrochem. Soc.* **1998**, *145*, 2971.
[4] K. Terabe, T. Hasegaw, T. Nakayama, M. Aono, *Riken Rev* **2001**, *37*, 7.
[5] M. N. Kozicki, M. Yun, L. Hilt, A. Singh, In *Proceed. Internat. Solid-State Ionic Devices Conf., Seattle, WA, USA, 02/05/1999-07/05/1999*. Center for Solid State Electron Res, Arizona State Univ, Tempe, AZ, USA, Electrochem. Soc, **1999**, pp. 298–309.
[6] I. Shimizu, H. Kokado, E. Inoue, *Bull. Chem. Soc. Jpn.* **1973**, *46*, 3662.
[7] Y. Hirose, H. Hirose, *J. Appl. Phys.* **1976**, *47*, 2767.
[8] D. Jana, S. Roy, R. Panja, M. Dutta, S. Z. Rahaman, R. Mahapatra, S. Maikap, *Nanoscale res. lett.* **2015**, *10*, 188.
[9] J. Song, J. Woo, A. Prakash, D. Lee, H. Hwang, *IEEE Electron Dev. Lett.* **2015**, *36*, 681.
[10] J. S. Meena, S. M. Sze, U. Chand, T. Tseng, *Nanoscale Res. Lett.* **2014**, *9*, 1.
[11] M. Luebben, S. Menzel, S. G. Park, M. Yang, R.Waser, I. Valov, *Nanotechnology* **2017**, *28*, 135205.
[12] S. A. Chekol, F. Cüppers, R. Waser, S. Hoffmann-Eifert, in *2021 IEEE International Memory Workshop (IMW)*. IEEE International Memory Workshop (IMW), IEEE, Piscataway, NJ **2021**, pp. 1–4.
[13] L. Völkel, D. Braun, M. Belete, S. Kataria, T. Wahlbrink, K. Ran, K. Kistermann, J. Mayer, S. Menzel, A. Daus, M. C. Lemme, *Adv. Funct. Mater.* **2024**, *34*, 2300428.
[14] S. Lee, J. Song, S. Lim, S. A. Chekol, H. Hwang, *Solid-State Electron.* **2019**, *153*, 8.
[15] C. Hsu, A. Saleem, A. Singh, D. Kumar, T. Tseng, *IEEE Transact. Electron Dev.* **2021**, *68*, 5578.
[16] A. Belmonte, A. Fantini, A. Redolfi, M. Houssa, M. Jurczak, L. Goux, *physica status solidi (a)* **2016**, *213*, 302.
[17] C. Schindler, *Resistive switching in electrochemical metallization memory cells*. Ph.D. thesis, Aachen, Techn. Hochsch., Diss **2009**.

[18] D. Ielmini, R. Waser, *Resistive Switching - From Fundamentals of Nanoionic Redox Processes to Memristive Device Applications*, Wiley-VCH, New York **2016**.
[19] H. Abbas, J. Li, D. S. Ang, *Micromachines* **2022**, *13*, 725.
[20] Y. Yang, P. Gao, L. Li, X. Pan, S. Tappertzhofen, S. Choi, R. Waser, I. Valov, W. D. Lu, *Nat. Commun.* **2014**, *5*, 4232.
[21] H. Abbas, Y. Abbas, G. Hassan, A. S. Sokolov, Y. R. Jeon, B. Ku, C. J. Kang, C. Choi, *Nanoscale* **2020**, *12*, 14120.
[22] T. S. Lee, N. J. Lee, H. Abbas, H. H. Lee, T. Yoon, C. J. Kang, *ACS Applied Electronic Materials* **2020**, *2*, 1154.
[23] H. Sun, Q. Liu, C. Li, S. Long, H. Lv, C. Bi, Z. Huo, L. Li, M. Liu, *Adv. Funct. Mater.* **2014**, *24*, 5679.
[24] M. Jin, L. Cheng, Y. Li, S. Hu, K. Lu, J. Chen, N. Duan, Z. Wang, Y. Zhou, T. Chang, X. Miao, *Nanotechnology* **2018**, *29*, 385203.
[25] C. Rebora, M. Bocquet, T. Ouled-Khachroum, M. Putero, D. Deleruyelle, 2014 10th Conference On Ph.d. Research in Microelectronics and Electronics (PRIME), IEEE **2014**, 1.
[26] A. Ali, H. Abbas, M. Hussain, S. H. A. Jaffery, S. Hussain, C. Choi, J. Jung, *Nano Res.* **2022**, *15*, 1.
[27] C. Pan, Y. Ji, N. Xiao, F. Hui, K. Tang, Y. Guo, X. Xie, F. M. Puglisi, L. Larcher, E. Miranda, L. Jiang, Y. Shi, I. Valov, P. McIntyre, R. Waser, M. Lanza, *Adv. Funct. Mater.* **2017**, *27*, 1604811.
[28] Y. Jeon, J. Choi, J. Kwon, M. H. Park, Y. Kim, C. Choi, *ACS Appl. Mater. Interf.* **2021**, *13*, 10161.
[29] S. Rehman, M. F. Khan, S. Aftab, H. Kim, J. Eom, D. Kim, *J. Mater. Chem. C* **2019**, *7*, 725.
[30] M. Zhao, S. Wang, D. Li, R. Wang, F. Li, M. Wu, K. Liang, H. Ren, X. Zheng, C. Guo, X. Ma, B. Zhu, H. Wang, Y. Hao, *Adv. Electron. Mater.* **2022**, *8*, 2101139.
[31] T. Hussain, H. Abbas, C. Youn, H. Lee, T. Boynazarov, B. Ku, Y. Jeon, H. Han, J. H. Lee, C. Choi, T. Choi, *Adv. Mater. Technol.* **2022**, *7*, 2100744.
[32] X. Xu, H. Lv, H. Liu, Q. Luo, T. Gong, M. Wang, G. Wang, M. Zhang, Y. Li, Q. Liu, S. Long, M. Liu, *Nanoscale Res. Lett.* **2015**, *10*, 61.
[33] G. Molas, J. Guy, M. Barci, F. Longnos, G. Palma, E. Vianello, P. Blaise, B. D. Salvo, L. Perniola, in *2015 International Conference on Solid State Devices and Materials (SSDM)*., The Japan Society of Applied Physics, Sapporo, Japan **2015**.
[34] M. Kund, G. Beitel, C.-U. Pinnow, T. Rohr, J. Schumann, R. Symanczyk, K.-D. Ufert, G. Muller, in *IEEE International Electron Devices Meeting, 2005. IEDM Technical Digest*. IEEE, Piscataway, NJ **2005**, pp. 754–757.
[35] S. Dietrich, M. Angerbauer, M. Ivanov, D. Gogl, H. Hoenigschmid, M. Kund, C. Liaw, M. Markert, R. Symanczyk, L. Altimime, S. Bournat, G. Mueller, *IEEE J. Solid-State Circuits* **2007**, *42*, 839.
[36] J. Jameson, P. Blanchard, C. Cheng, J. Dinh, A. Gallo, V. Gopalakrishnan, C. Gopalan, B. Guichet, S. Hsu, D. Kamalanathan, D. Kim, F. Koushan, M. Kwan, K. Law, D. Lewis, Y. Ma, V. Mccaffrey, S. Park, S. Puthenthermadam, E. Runnion, J. Sanchez, J. Shields, K. Tsai, A. Tysdal, D. Wang, R. Williams, M. N. Kozicki, J. Wang, V. Gopinath, S. Hollmer, M. Van Buskirk, in *2013 IEEE International Electron Devices Meeting*. IEEE, Piscataway, NJ **2013**, pp. 1–30.
[37] R. Waser, R. Dittmann, G. Staikov, K. Szot, *Adv. Mater.* **2009**, *21*, 2632.
[38] Y. Yang, P. Gao, S. Gaba, T. Chang, X. Pan, W. Lu, *Nat. Commun.* **2012**, *3*, 732.
[39] S. Tappertzhofen, I. Valov, R. Waser, *Nanotechnology* **2012**, *23*, 145703.
[40] T. Tsuruoka, T. Hasegawa, K. Terabe, M, Aono, *Nanotechnology* **2012**, *23*, 435705.
[41] J. R. Jameson, N. Gilbert, F. Koushan, J. Saenz, J. Wang, S. Hollmer, M. Kozicki, N. Derhacobian, *IEEE Electron Device Lett.* **2012**, *33*, 257.
[42] S. Menzel, U. Böttger, R. Waser, *J. Appl. Phys.* **2012**, *111*, 014501.
[43] S. Ambrogio, S. Balatti, S. Choi, D. Ielmini, *Advanced Materials* **2014**, *26*, 3885.
[44] S. Menzel, N. Adler, J. van den Hurk, S. Tappertzhofen, I. Valov, R. Waser, in *2013 5th IEEE International Memory Workshop (IMW), 26-29 May 2013, Taipeh, Taiwan* **2013**, pp. 92–95.
[45] M. Buttberg, I. Valov, S. Menzel, *Neuromorphic Computing and Engineering* **2023**, *3*, 024010.
[46] S. A. Chekol, S. Menzel, R. W. Ahmad, R. Waser, S. Hoffmann-Eifert, *Adv. Funct. Mater.* **2021**, *32*, 2111242.
[47] R. D. Nikam, K. G. Rajput, H. Hwang, *Small* **2021**, *17*, 2006760.
[48] S. Menzel, *Journal of Computational Electronics* **2017**, *16*, 1017.
[49] W. Wang, M. Wang, E. Ambrosi, A. Bricalli, M. Laudato, Z. Sun, X. Chen, D. Ielmini, *Nature Communications* **2019**, *10*, 81.
[50] Y. Zhao, P. Huang, Z. Zhou, C. Li, S. Qin, L. Liu, X. Liu, H. P. Wong, J. Kang, *IEEE Electron Device Lett.* **2019**, *40*, 647.
[51] S. Menzel, P. Kaupmann, R. Waser, *Nanoscale* **2015**, *7*, 12673.
[52] S. Qin, Z. Liu, G. Zhang, J. Zhang, Y. Sun, H. Wu, H. Qian, Z. Yu, *Phys. Chem. Chem. Phys.* **2015**, *17*, 8627.
[53] J. Aeschlimann, F. Ducry, C. Weilenmann, J. Leuthold, A. Emboras, M. Luisier, *Phys. Rev. A: At. Mol. Opt. Phys.* **2023**, *19*, 24.
[54] S. Yu, H.-S. Wong, *IEEE Trans. Electron Devices* **2011**, *58*, 1352.
[55] S. Menzel, S. Tappertzhofen, R. Waser, I. Valov, *PCCP* **2013**, *15*, 6945.
[56] D. Ielmini, S. Balatti, S. Larentis, *Jpn. J. Appl. Phys.* **2013**, *52*, 04CD10.
[57] Z. Wang, S. Joshi, S. E. Savel'ev, H. Jiang, R. Midya, P. Lin, M. Hu, N. Ge, J. P. Strachan, Z. Li, Q. Wu, M. Barne, G. Li, H. L. Xin, R. S. Williams, Q. Xia, J. J. Yang, *Nat. Mater.* **2017**, *16*, 101.
[58] U. Celano, L. Goux, A. Belmonte, K. Opsomer, A. Franquet, A. Schulze, C. Detavernier, O. Richard, H. Bender, M. Jurczak, W. Vandervorst, *Nano Letters* **2014**, *14*, 2401.
[59] Y. Takahashi, M. Kudo, I. Fujiwara, M. Shimuta, K. Ohba, M. Arita, in *2015 IEEE International Memory Workshop (IMW)*., IEEE, Piscataway, NJ **2015**, pp. 1–4.
[60] F. Yuan, Z. Zhang, C. Liu, F. Zhou, H. M. Yau, W. Lu, X. Qiu, H.-S. P. Wong, J. Dai, Y. Chai, *ACS Nano* **2017**, *11*, 4097.
[61] X. Guo, C. Schindler, S. Menzel, R. Waser, *Appl. Phys. Lett.* **2007**, *91*, 1.
[62] S. Rajabi, M. Saremi, H. Barnaby, A. Edwards, M. Kozicki, M. Mitkova, D. Mahalanabis, Y. Gonzalez-Velo, A. Mahmud, *Solid-State Electronics* **2015**, *106*, 27.
[63] A. Belmonte, U. Celano, A. Redolfi, A. Fantini, R. Muller, W. Vandervorst, M. Houssa, M. Jurczak, L. Goux, *IEEE Trans. Electron Devices* **2015**, *62*, 2007.
[64] S. Menzel, U. Böttger, M. Wimmer, M. Salinga, *Adv. Funct. Mater.* **2015**, *25*, 6306.
[65] I. Valov, R. Waser, J. R. Jameson, M. N. Kozicki, *Nanotechnology* **2011**, *22*, 254003.
[66] C. H. Hamann, A. Hamnett, W. Vielstich, *Electrochemistry*, 2 ed., Wiley-VCH, Weinheim **2007**.
[67] E. J. F. Dickinson, A. J. Wain, *J. Electroanalyt. Chem.* **2020**, *872*, 114145.
[68] N. F. Mott, R. W. Gurney, *Electronic processes in ionic crystals*, Oxford Univ. Press, London, U.K., **1948**.
[69] J. O'Dwyer, *The Theory of Electrical Conduction and Breakdown in Solid Dielectrics, Clarendon Press, Oxford*, Clarendon Press, Oxford **1973**.
[70] J. G. Simmons. in, *J. Appl. Phys.* **1963**, *34*, 238.
[71] N. Matthews, M. J. Hagmann, A. Mayer, *J. Appl. Phys.* **2018**, *123*, 1793.
[72] Cambridge University Press, *The conductivity of thin metallic films according to the electron theory of metals*, vol. *34*, Mathematical Proceedings of the Cambridge Philosophical Society, Cambridge **1938**.
[73] E. H. Sondheimer, *Adv. Phys.* **1952**, *1*, 1.
[74] T. Hennen, E. Wichmann, A. Elias, J. Lille, O. Mosendz, R. Waser, D. Wouters, D. Bedau, *Rev. Sci. Instrum.* **2021**, *92*, 054701.
[75] Y. S. Ju, *The Ninth Intersociety Conf. Thermal Thermomechan. Phenom. Electron. Syst. IEEE* **2004**, *2*, 411.
[76] R. Cao, S. Liu, Q. Liu, X. Zhao, W. Wang, X. Zhang, F. Wu, Q. Wu, Y. Wang, H. Lv, S. Long, M. Liu, *IEEE Electron Device Lett.* **2017**, *38*, 1371.

[77] A. Ali, H. Abbas, M. Hussain, S. H. A. Jaffery, S. Hussain, C. Choi, J. Jung, *Appl. Mater. Today* **2022**, *29*, 101554.
[78] L. Goux, J. Radhakrishnan, A. Belmonte, T. Witters, W. Devulder, A. Redolfi, S. Kundu, M. Houssa, G. S. Kar, *Faraday Discuss.* **2019**, *213*, 67.
[79] X. Zhao, S. Liu, J. Niu, L. Liao, Q. Liu, X. Xiao, H. Lv, S. Long, W. Banerjee, W. Li, S. Si, M. Liu, *Small* **2017**, *13*, 1603948.
[80] Y. Sun, H. Xu, S. Liu, B. Song, H. Liu, Q. Liu, Q. Li, *IEEE Electron Device Lett.* **2018**, *39*, 492.
[81] Y. Choi, S. Bang, T. Kim, K. Hong, S. Kim, S. Kim, B. Park, W. Y. Choi, *ACS Appl. Electron. Mater.* **2023**, *5*, 1834.
[82] J. van den Hurk, S. Menzel, R. Waser, I. Valov, *J. Phys. Chem. C* **2015**, *119*, 18678.
[83] F. Longnos, E. Vianello, G. Molas, G. Palma, E. Souchier, C. Carabasse, M. Bernard, B. D. Salvo, D. Bretegnier, J. Liebault, in *2013 5th IEEE International Memory Workshop*. IEEE, Piscataway, NJ **2013**, pp. 96–99.
[84] J. Yoo, J. Park, J. Song, S. Lim, H. Hwang, *Appl. Phys. Lett.* **2017**, *111*, 63109.
[85] Y. Wang, Z. Zhang, H. Li, L. Shi, *Journal of Electronic Materials* **2019**, *48*, 517.
[86] Y. Zhao, C. Fang, X. Zhang, X. Xu, T. Gong, Q. Luo, C. Chen, Q. Liu, H. Lv, Q. Li, F. Zhang, L. Li, M. Liu, *IEEE Trans. Electron Devices* **2018**, *65*, 4290.
[87] J. Yin, F. Zeng, Q. Wan, Y. Sun, Y. Hu, J. Liu, G. Li, F. Pan, *J. Phys. Chem. C* **2019**, *123*, 878.
[88] X. Zhao, J. Ma, X. Xiao, Q. Liu, L. Shao, D. Chen, S. Liu, J. Niu, X. Zhang, Y. Wang, R. Cao, W. Wang, Z. Di, H. Lv, S. Long, M. Liu, *Adv. Mater.* **2018**, *30*, 1705193.
[89] Y. Li, J. Tang, B. Gao, W. Sun, Q. Hua, W. Zhang, X. Li, W. Zhang, H. Qian, H. Wu, *Adv. Sci.* **2020**, *7*, 2002251.